Polymer 230 (2021) 124035

Contents lists available at ScienceDirect

Polymer

journal homepage: www.elsevier.com/locate/polymer

Injection vs micro-injection molding of nano-particle filled polyamide 6: Moldability and structuring

Rossella Surace [a], Claudia Pagano [b,*], Vincenzo Bellantone [a], Simone Gatti [c], Leonardo Castellani [d], Massimo Vighi [d], Grégory Stoclet [e], Sara Sechi [f], Irene Fassi [b], Francesco Baldi [b,f]

[a] STIIMA-CNR, Institute of Intelligent Industrial Systems and Technologies for Advanced Manufacturing, Consiglio Nazionale delle Ricerche, Via Lembo 38/F, I-70124, Bari, Italy
[b] STIIMA-CNR, Institute of Intelligent Industrial Systems and Technologies for Advanced Manufacturing, Consiglio Nazionale delle Ricerche, Via Corti 12, I-20133, Milano, Italy
[c] Radici Novacips S.p.A. Via Provinciale 1331, I-24020, Villa d'Ogna, Bergamo, Italy
[d] Versalis S.p.A. Basic Chemicals and Plastics Research Center, Via Taliercio 14, I-46100, Mantova, Italy
[e] Univ. Lille, CNRS, INRAE, Centrale Lille, UMR 8207 - UMET - Unité Matériaux et Transformations, F-59000, Lille, France
[f] Università degli Studi di Brescia, Dipartimento di Ingegneria Meccanica e Industriale, Via Branze 38, I-25123, Brescia, Italy

ARTICLE INFO

Keywords:
Polyamide 6
Carbon nanotubes
Silicate layers
Nanocomposites
Micro-injection molding
Structural characterization
Morphological characterization
Calorimetric characterization

ABSTRACT

In this work, the moldability via micro-injection molding (μIM) of nano-filled polyamide 6 (PA6) based systems and the microstructural characteristics of the micro-injected parts were investigated and compared to those observed via traditional injection molding (IM). Two types of nano-fillers, different in nature and geometry, were examined, namely carbon nanotubes and silicate layers. The presence of nano-fillers did not impair the mold replication capability of PA6 in the μIM process. A micro-rib and a standard dumbbell specimen for tensile tests were used as reference micro- and macro-injected part, respectively. Transmission Electron Microscopy, Wide and Small Angle X-ray Scattering and Differential Scanning Calorimetry analyses showed that, due to the different thermomechanical histories during μIM and IM, the micro- and the macro-parts have different micro-structures, influenced also by the filler type. Both nano-filler dispersion and PA6 crystallinity were influenced.

1. Introduction

Injection molding, IM, is probably the most used technique to manufacture thermoplastic polymeric products. In an IM cycle, a polymer melt is forced to flow under high pressure into a mold, where the polymer solidifies in the desired shape and size. As known, polymer processing does not involve only shaping, but also material structuring, and in the case of IM this results in microstructural complexity and inhomogeneity along the part thickness and at different points of the molded piece, which depends on material, part geometry and processing conditions. It is generally accepted that the differences in cooling rate between the external layer of the molded part and its central portion produces a skin-core-skin structure [1]. For thermoplastic semi-crystalline polymers filled with rigid particles with aspect ratio higher than 1, skin and core of a molded part can differ in both the crystallinity and the macromolecular orientation of the polymer matrix as well as in the orientation of the particles (see, for example [2–5]). This is the case of thermoplastic polymer-based composites typically used in engineering applications. These systems, generally obtained by melt compounding (they are fully-fledged compounds), consist in a polymer matrix in which either micro- or nano-particles, or even both together in hybrid systems, are dispersed. The most popular micro-fillers with high aspect ratio used in industrial compounds are the discontinuous fibers (of glass, carbon, basalt etc.), which are added to polymers in order to obtain thermoplastic materials with enhanced mechanical and thermal properties with respect to the base polymers. Concerning nano-particles, their use as fillers in polymer composites has been the object of many studies in the past few decades (ref. to the reviews [6,7]). To be properly considered "nano", these particles must have at least one dimension of nanometer range. High aspect ratio nano-particles can be one-dimensional, 1D (such as the carbon nanotubes), or two-dimensional, 2D (such as the silicate or the graphene layers). Due to

* Corresponding author.
E-mail address: claudia.pagano@stiima.cnr.it (C. Pagano).

https://doi.org/10.1016/j.polymer.2021.124035
Received 17 March 2021; Received in revised form 12 July 2021; Accepted 16 July 2021
Available online 21 July 2021
0032-3861/© 2021 Elsevier Ltd. All rights reserved.

the exceptionally high specific surface area that they exhibit when properly dispersed within the polymer matrix, the addition of small amounts of nano-particles (typically less than 10 wt%) produces a significant improvement in a broad spectrum of properties. Even though nano-particles can have a reinforcement effect once incorporated into a polymer, they are particularly effective at inducing modifications in specific functional properties, such as thermal and electrical conductivity, reaction to fire, permeability, to an extent that depends on the characteristics of the specific system considered. Interestingly, their effects are often related to their effect on the crystalline structure of the polymer [8–11].

While in micro-composites, the presence of the fillers often impair the processability via IM, in nano-composites the processability of the material is just slightly modified, with respect to the polymer matrix, due to the addition of relatively small quantities of nano-particles (see, for example: [12–14]. This makes the nano-composites ideal candidates for manufacturing high value miniaturized components by means of micro-injection molding (μIM). μIM is one of the key manufacturing technologies for the mass production of miniaturized components in thermoplastic polymers with applications in several industrial fields, such as biomedical [15,16], optics [17,18], and high-precision mechanical industry [19–21]. With respect to the more traditional IM, in a generic μIM process the polymer melt is forced to flow in non-isothermal conditions at much higher shear rates through channels characterized by higher surface to volume ratios. This results in different thermo-mechanical histories undergone by the material, which can give rise to particularly complex micro-structures [22–28], especially when high aspect ratio rigid fillers are dispersed within a semi-crystalline polymer [29,30].

In this work, the moldability via μIM of nano-filled polyamide 6 (PA6) based systems and the microstructural characteristics of the micro-parts were investigated and compared with those observed via traditional IM. PA6 is a semi-crystalline thermoplastic polymer frequently chosen as matrix in high performance polymer-based composites. The nano-composites examined, prepared by melt compounding, had the same nominal filler weight-content (≈7 wt%), but a differed type of nano-fillers. Relatively high aspect ratio 1D and 2D nano-fillers were examined, namely multiwalled carbon nanotubes and silicate layers from organo-modified montmorillonite. The commercial PA6 was also examined. In order to compare μIM with IM, reference micro- and macro-samples were molded. The reference micro-sample consisted in a rib, having nominal cross-section of 0.03 mm^2, while a dumbbell specimen for mechanical tensile tests, with central narrow portion having nominal cross-section of 40 mm^2, was selected as the reference macro-sample. The material microstructure in the micro- and macro-parts was investigated by means of morphological analyses by Transmission Electron Microscopy (TEM), structural analyses by Wide and Small Angle X-ray Scattering (WAXS and SAXS) and calorimetric analyses by Differential Scanning Calorimetry (DSC).

2. Experimental

2.1. Materials and parts

2.1.1. Materials and compounding

A low-viscosity grade of PA6, suitable for μIM processes, was supplied by Radici Novacips S.p.A. (Villa d'Ogna, Bergamo, Italy) as pellets. It has a density in the solid state of 1.140 g/cm^3, and melting temperature of 220 °C (data from the manufacturer). The organo-clay (MMT) was Dellite 67G from Laviosa Chimica Mineraria SpA (Livorno, Italy), it is an alkyl quaternary ammonium montmorillonite containing about 55 ÷ 60 wt% clay. The average size of the organo-clay particles is 8 μm, and the apparent density of the powder is 0.45 g/cm^3. The multiwalled carbon nanotubes (CNT) were Baytubes C150P from Bayer MaterialScience (Germany), with an average length of ≈770 nm and diameter of ≈10 nm.

The compounding process was performed using an intermeshing co-rotating twin-screw extruder (micro-extruder by LabTech), with a screw diameter of 16 mm and length-to-screw diameter ratio of 40 [31]. Before extrusion the PA6 pellets were pre-dried for at least 3 h at 95 °C, according to the manufacturer recommendation. The nanotubes were fed together with the polymer pellets into the extruder throat, while the organo-clay particles were added in the side-feeder zone. Volumetric dosing units were employed after a proper calibration, in order to obtain a filler content of ≈7 wt% for both the fillers. The processing conditions were kept fixed: screw rotation speed of 150 RPM, feed rate of 2.5 kg/h, barrel temperatures set to 190 °C in the feeding zone and gradually increased up to 240 °C in the die zone. Once steady-state extrusion conditions were reached, the extruded strands were pelletized for the following molding processes. The actual filler content in the composites was verified by means of thermogravimetric analyses performed on the granules, under a nitrogen atmosphere by using a TA Instruments analyzer (model Q500). For the determination of the MMT content, the nominal content of clay in the organo-clay was used.

Codes PA6-MMT and PA6-CNT are used in the paper to indicate the composites containing MMT and CNT, respectively.

2.1.2. Parts and molds

The micro-part examined is a rib of a molded sample that contains five nominally identical ribs (see Fig. 1a). Fig. 1a also shows the drawing of the mold used to manufacture the micro-parts. The mold is a double-impression mold in Ni–Cr–Mo steel manufactured by a micro-milling machine (KERN Evo). The master mold has two inserts with the micro-channels for the ribs located in the central position and machined by micro Electrical Discharge Machining (EDM). The average roughness of the channels was equal to 0.4 ± 0.05 μm. The rib channel in the mold has length of 2 mm, trapezoidal section with minor and major bases of 100 and 200 μm, respectively, and thickness equal to 200 μm.

The macro-part examined is a dumbbell specimen for tensile tests according to ISO 527 [32] (see Fig. 1b). The mold used is a double-impression mold. Fig. 1b also shows the drawing of the macro-part cavity. The central narrow portion has nominal length of 80 mm, thickness of 4 mm and width of 10 mm. The necessity of 1° draft angle makes trapezoidal the actual cross-section of the cavity.

2.1.3. Injection molding processes

The IM process was performed by a Sumitomo Demag Systec 100/420–430 hydraulic machine having screw diameter of 40 mm and maximum shot weight of 205 g [33]. All the materials (PA6, PA6-MMT and PA6-CNT) were processed with the same process parameters, obtaining regular quality macro-parts. Polymer melt and mold temperatures were set at 250 °C and 70 °C, respectively. The injection velocity, holding pressure and holding time were set at the following values: 30 mm/s, 40 bar and 7 s.

The μIM process was performed by a DesmaTec FormicaPlast 1K machine, whose architecture is characterized by two pistons: a 6 mm diameter one for the pre-plasticization phase and a 3 mm diameter one for the injection. This machine has a maximum injection volume of 150 mm^3 and is particularly accurate for melt metering and for avoiding materials degradation. Detailed description of the machine and process is provided in Ref. [34]. μIM tests were performed in a climatic chamber, at 20 °C and 50 % relative humidity. In contrast to IM, it was necessary to vary the process parameters depending on the material examined to obtain regular quality micro-parts. Therefore, to select the process conditions for the micro-parts (used for the microstructural characterization), a specific screening analysis was carried out (see section 3.1).

Before the injection processes, the materials were pre-dried following the same procedure adopted for the compounding and described in section 2.1.1.

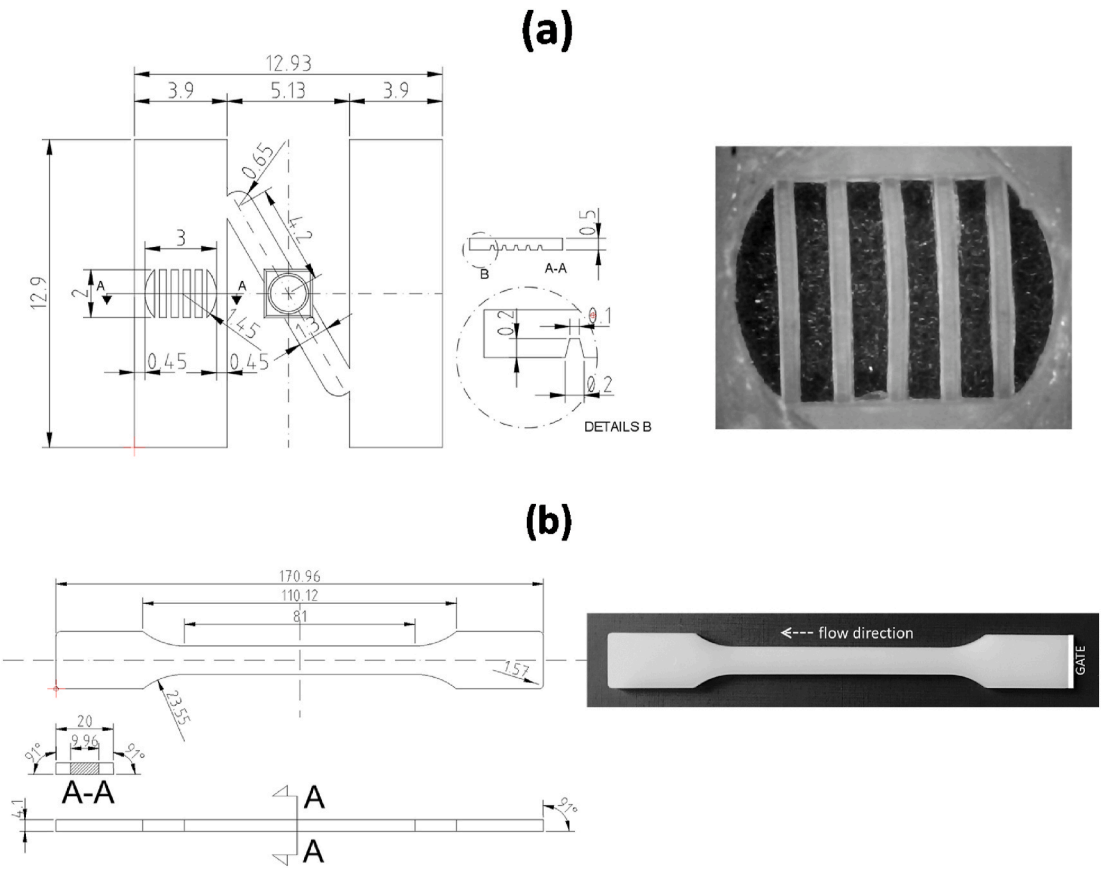

Fig. 1. Mold drawing and part photo of (**a**) the micro-part and (**b**) the macro-part. In (**b**), the drawing of one single cavity is reported. Dimensions are in mm.

2.2. Characterization

2.2.1. Dimensional accuracy tests

Polymer moldability is defined as the capability to replicate the nominal feature dimensions [35]. Based on the definition of molding shrinkage from the standard ISO 294–4 [36], the quality index for the analysis of micro-parts was defined as the relative measured difference between mold and part:

$$DAI = \left(\frac{L_m - L_p}{L_m}\right) \times 100 \quad (1)$$

where L_m and L_p are the length of the selected feature of mold and part, respectively. This parameter has been named Dimensional Accuracy Index (DAI). The lower the value of DAI, the higher the capability to replicate the mold dimensions. The length of the minor base of the trapezoidal cross-section of the rib was used as reference length for the mold (L_m = 100 μm from Fig. 1a details B). For the measurement of L_p (see Fig. 2) images of the samples were acquired by a confocal microscopy Zeiss AxioVision with magnification of 275x and a resolution on x-y plane of 0.9 μm. The central rib of five different samples were measured (Fig. 2) and the average value used as L_p for the DAI evaluation. These measurements were carried out for each material about 24 h after molding.

DAI values were also determined for the macro-parts. In analogy to micro-part DAI determination, the length of the minor base of the trapezoidal cross-section of central narrow portion of the dumbbell specimen was used as reference length (L_m = 9.96 mm). L_p was measured at three different positions of five macro-samples using an optical travelling microscope by Leica, with measurement graduation of 1 μm. Average L_p values were then used for DAI evaluation. These measurements were carried out for each material about 12 months after molding, during which the parts were kept into multi-layer aluminum-polyethylene double wrapped bags to limit water uptake.

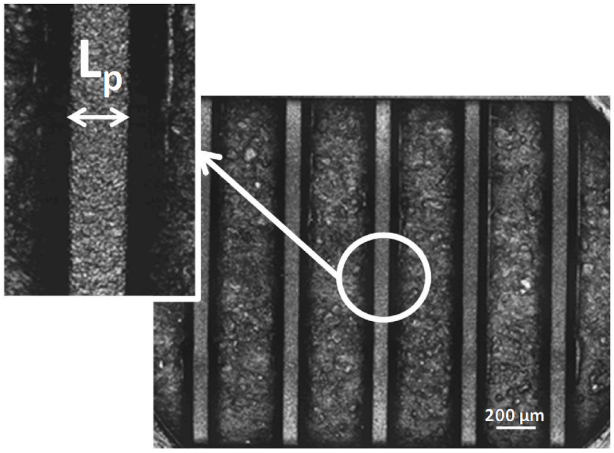

Fig. 2. Details of the measurement of L_p on a micro-part, for DAI evaluation (see text).

2.2.2. Morphological analyses

TEM analysis was carried out on a FEI CM 120 microscope operated under an acceleration voltage of 80 kV and with a reduced spot size in order to minimize damage of the sample during the observations. Samples with thickness of about 100 nm were cut at room temperature, from the rib and the central narrow portion of the dumbbell specimen, by a Leica EM UC7 ultra-microtome, in such a way that the sample plane was perpendicular to the injection flow direction.

WAXS and SAXS measurements were performed on a Xeuss 2.0 apparatus (Xenocs) equipped with a microsource using Cu Kα radiation (λ = 1.54 Å) and point collimation (beam size: 300 × 300 μm^2). The sample to detector distance, around 0.15 m for WAXS and 1.20 m for SAXS, was calibrated using silver behenate as a standard. The WAXS and SAXS analyses were performed in transmission mode and the patterns were recorded on a Pilatus detector (Dectris). The intensity profiles were obtained by azimuthal integration of the 2D patterns. Standard corrections (dark subtraction, empty beam correction, etc.) were applied before performing any treatment to the obtained patterns. For the macro-part, an average diffractogram was constructed from the normalized intensity profiles recorded along three orthogonal directions. More precisely, 1 mm thick samples were cut from the central narrow section of the dumbbell and analyzed along "face-on", "edge-on" and "through-on" directions, as depicted in Fig. 3. The average integrated intensity profile was then constructed as the sum of the three intensity profiles divided by 3. For the micro-part, due to their very small size and assuming a cylindrical symmetry regarding the structure, the ribs were analyzed along the "face-on" direction.

Structural characterization by means of WAXS during heating and cooling of the samples was also carried out. WAXS patterns were recorded in-situ (acquisition duration: 30 s), during the thermal treatments, performed with a HFSX350 temperature stage (Linkam). The 1 mm thick specimens cut from the macro-parts were heated from 25 °C to 270 °C, and then cooled down, at a rate of 5 °C/min.

Finally, the raw organo-clay (MMT) powder was also analyzed by means of WAXS in transmission mode using the same testing conditions adopted for the polymer samples.

2.2.3. Calorimetric analyses

DSC analyses were performed with a Mettler Toledo calorimeter (model DSC1). For the macro-part a sample of ≈10 mg was taken from the middle of the central narrow section of the dumbbell, far from the external surface so that the sample was representative of the part core. For the analyses of the μIM, the ribs of several micro-parts were collected to obtain DSC samples with a mass of ≈5 mg. The samples were heated from 40 °C to 260 °C at 10 °C/min, under a nitrogen atmosphere in order to prevent oxidation. Heating scans were analyzed in the range of the melting temperature. For each material/part combination, the test was repeated at least three times.

3. Results and discussion

3.1. Moldability

The analysis of the moldability via μIM was divided into two phases: a screening phase to determine the working technological window for each material and define the whole set of process conditions to obtain micro-parts with the best quality; a dimensional accuracy measurement phase on micro-parts obtained with the selected process conditions.

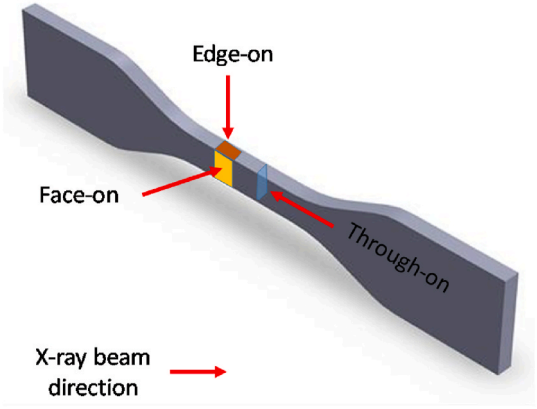

Fig. 3. Details of the experimental procedure adopted for the X-ray characterization of macro-parts (see text).

The screening phase involved the process parameters which affect greatly the performance of the process [37,38] and have a direct impact on replicating capability [35], namely the polymer melt (T_m), mold temperatures (T_{mo}), injection velocity (v_{inj}), holding pressure (P_h) and time (t_h). Firstly, the values of process parameters were selected based on previous experimentations [39,40]; then, the operative window was tested evaluating the part filling (complete or not), flash formation and other defects to select the optimized values and define the process conditions, reported in Table 1. Fig. 4 shows some examples of defective parts with flashes and/or incomplete ribs. The other process parameters were kept fixed at the following values: piston run (it is the moving path of the injection piston that defines the injected volume of material) set at 8.5 mm, and the cooling time set at 5 s.

As shown in Table 1 the "reference" T_m is the same for all the materials, while T_{mo} is slightly lower for PA6-MMT. v_{inj} promotes the flow progress in cavities, which is of paramount importance especially in high aspect ratio cavities, and greatly affects the part quality and, consequently, the dimensional accuracy of the product [35]. High v_{inj} reduces the filling time and the occurrence of incomplete filling, due to the early solidification of the melt. Interestingly, the present analysis evidences that optimal velocity is quite different for each tested material, increasing from a minimum value for neat PA6 (150 mm/s) to a maximum for PA6-CNT (330 mm/s). Significant differences in the optimal value of P_h can be also noticed. However, the holding pressure, applied after the filling phase to compensate for the polymer cooling shrinkage, plays only a secondary role in the quality of the ribs [35], due to the high aspect ratio of the part. The differences observed for v_{inj} and P_h should be related to the different thermo-rheological responses of the three materials here examined, which are, however, likely to be too small to produce a significant effect on the moldability via IM. This hypothesis is also supported by the different thermo-mechanical histories experienced by the materials during the IM and the μIM. Indeed, the lateral surface to volume ratio of the micro-part (rib) is more than 30 times higher than that of the central narrow section of the macro-part. Moreover, the maximum shear rate undergone by the polymer melt during the injection phase (at the wall of the mold cavity) in IM and μIM processes differ of more than one order of magnitude. Assuming that: i) the material is incompressible; ii) the material exhibits a power-law type constitutive behavior with exponent n = 0.5 (supported by the analysis of the neat PA6 flow curves provided by the manufacturer), and based on the geometry and process conditions the shear rate values at the wall of the mold cavity are: ≈ 1000 s^{-1} for the macro-part, in the central zone corresponding to the narrow section of the dumbbell specimen and ≈45000 s^{-1}, ≈72000 s^{-1} and ≈99000 s^{-1} for PA6, PA6-MMT and PA6-CNT micro-part, respectively.

DAI values determined for the micro-parts of the various materials processed according to the process conditions of Table 1 are reported in Table 2. The mean values for micro-parts are substantially the same regardless the material, whereas the standard deviation presents some differences. More specifically, a higher degree of scattering is observed for the composites. The presence of the nano-fillers might reduce the homogeneity of the flow during filling. Nevertheless, the results clearly show that the presence of nano-fillers in the nanocomposites does not

Table 1
Process conditions for micro-parts.

Process parameter	Neat PA6	PA6-MMT	PA6-CNT
T_m [°C]	250	250	250
T_{mo} [°C]	100	90	100
v_{inj} [mm/s]	150	240	330
P_h [bar]	500	600	100
t_h [s]	1	1	1

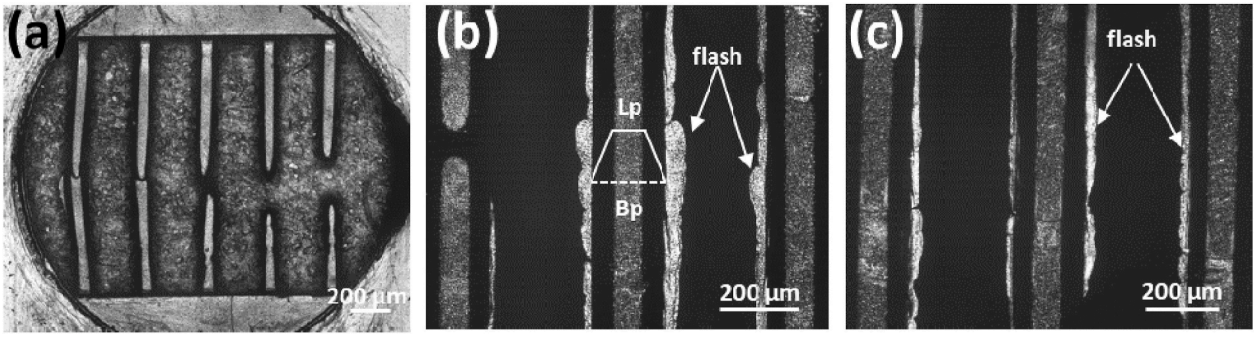

Fig. 4. Examples of defective micro-parts: (**a**) uncompleted rib; (**b**) uncompleted rib and flash (L_p and B_p represent the bases of the rib, which, as shown in Fig. 1 details B, has a trapezoidal shape); (**c**) flash.

Table 2
Dimensional Accuracy Index (DAI) values determined from tests on micro-parts and macro-parts of the various materials. For each combination of material/part type, the mean value ± standard deviation, SD, is also reported.

Sample	DAI [%]					
	micro-parts			macro-parts		
	Neat PA6	PA6-MMT	PA6-CNT	Neat PA6	PA6-MMT	PA6-CNT
#1	1.9	2.1	0.1	0.753	−0.154[a]	2.620
#2	1.5	−0.6[a]	3.1	0.763	1.191	2.550
#3	1.2	0.6	2.5	0.000	1.024	2.557
#4	1.4	0.5	0.9	0.365	1.017	2.661
#5	0.6	3.4	−0.2[a]	0.378	0.863	2.631
mean value ±SD	**1.3 ± 0.5**	**1.2 ± 1.5**	**1.2 ± 1.5**	**0.45 ± 0.32**	**0.79 ± 0.54**	**2.60 ± 0.05**

[a] Part appears larger than the corresponding mold dimension.

impair the mold replication capability of PA6, which, with the optimized process conditions, results very high. Indeed, although the high standard deviation values, this result is very satisfactory compared with other materials previously tested [35].

The negative values reported in Table 2 are due to measurements of the part larger than the corresponding mold dimension measurement; however, the difference between these measurements is below the instrumental resolution and, thus, within the experimental error.

Table 2 also shows DAI values of the macro-parts. The results indicate a high replication capability also for these parts. PA6-CNT shows a lower replication capability with respect to neat PA6 and PA6-MMT, not observed for the micro-parts. However, DAI values of the macro- and micro-part cannot be directly compared due to the possible different moisture content in the materials. The analysis of these results would require a comprehensive study of the thermo-rheological and volumetric behavior of the materials, which can be the object of future developments.

3.2. Structuring

3.2.1. Morphology and structure

TEM images obtained from macro- and micro-part of PA6-CNT and PA6-MMT are presented in Figs. 5 and 6, respectively. Fig. 5 clearly shows that, CNT are homogenously dispersed within the PA6 matrix in both the macro- and the micro-part, with no appreciable difference. On the contrary, evident differences between the two part sizes emerge for PA6-MMT (Fig. 6). Comparing the lower magnification images of the two types of part (Fig. 6a vs 6c), a remarkably different degree of dispersion can be noticed. Organo-clay particles are on average much smaller in size in micro-parts, than in macro-parts, and the number of particles distributed per unit volume within the polymer appears markedly higher in micro-samples. Since all the parts have been obtained from the same compound pellets, the difference originates from the processes. The higher magnification images (Fig. 6e and f) of the micro-part confirm that the organo-clay is dispersed within the PA6 matrix both as highly anisotropic individual layers and as anisotropic tactoids (stacks of layers) with various sizes (number of lamellae per single stack). Evidently, during µIM the organo-clay particles embedded in the polymer melt are fragmented and exfoliated, obtaining a nano-structured composite characterized by a large polymer/clay interaction surface. This might be a direct consequence of the specific mechanical history experienced by the melt filling the rib-cavities. In order to reach the rib-cavity, the polymer melt is forced to flow through (in this order): the sprue, the runner, the slit channel that feed the five rib-cavities (Fig. 1a). It undergoes a shear flow, but also a converging flow at the rib-cavity entrance, which is a superposition of shear and elongational flows. Thus, the polymer melt is strongly stretched at high strain rate along the direction of the cavity axis affecting the filler dispersion. This is in agreement with the literature [41,42] which confirms that an elongational flow promotes silicate layer exfoliation and reduction of clay particle size. Further, it is worth recalling that a shear flow at high shear rate can promote exfoliation [12], and in the rib-cavity the polymer melt undergoes a very high shear rate (see section 3.1). In consideration of this, it is reasonable to think that the combined action of the converging flow at the rib-cavity entrance and the shear flow in the cavity is directly responsible for the nano-structure observed in the micro-part. By contrast, macro-molding is much less effective at promoting organo-clay fragmentation and exfoliation due to the absence of effective converging flows and the remarkably lower level of shear rate undergone by the polymer melt during the flow in the cavity.

Moreover, the organo-clay particles appear remarkably less clear in the macro-part pictures than in those taken from the micro-part (compare Fig. 6b with 6d) suggesting a different degree of orientation of the particles along the flow direction (that is orthogonal to the photo) for the two different types of parts. More specifically, the orientation degree of the particles along the flow direction would be higher in the micro-part than in the macro-part, resulting in a more edgewise view of silicate layers and stacks of layers (Fig. 6c and d) in the former part than in the latter. This might be directly related to the higher shear rates present in the micro-cavity. A local character should be attributed to the nearly 45° orientation observed for the clay particles in the micro-part in Fig. 6d.

Fig. 7 depicts the 2D WAXS patterns recorded for the macro- and micro-parts of neat and nano-filled PA6 (for the macro-parts, only the "face-on" pattern is reported). All of the macro-parts exhibit a mostly isotropic crystalline structure shown by presence of the diffraction rings. The differences regarding the macro-part patterns are ascribed to differences in the crystalline structure of PA6, discussed later. By contrast, for both neat PA6 and PA6-MMT micro-parts, a pronounced orientation of the crystalline phase is observed, as marked by the presence of the arcs, indicated by the arrows, and the absence of the rings characteristic

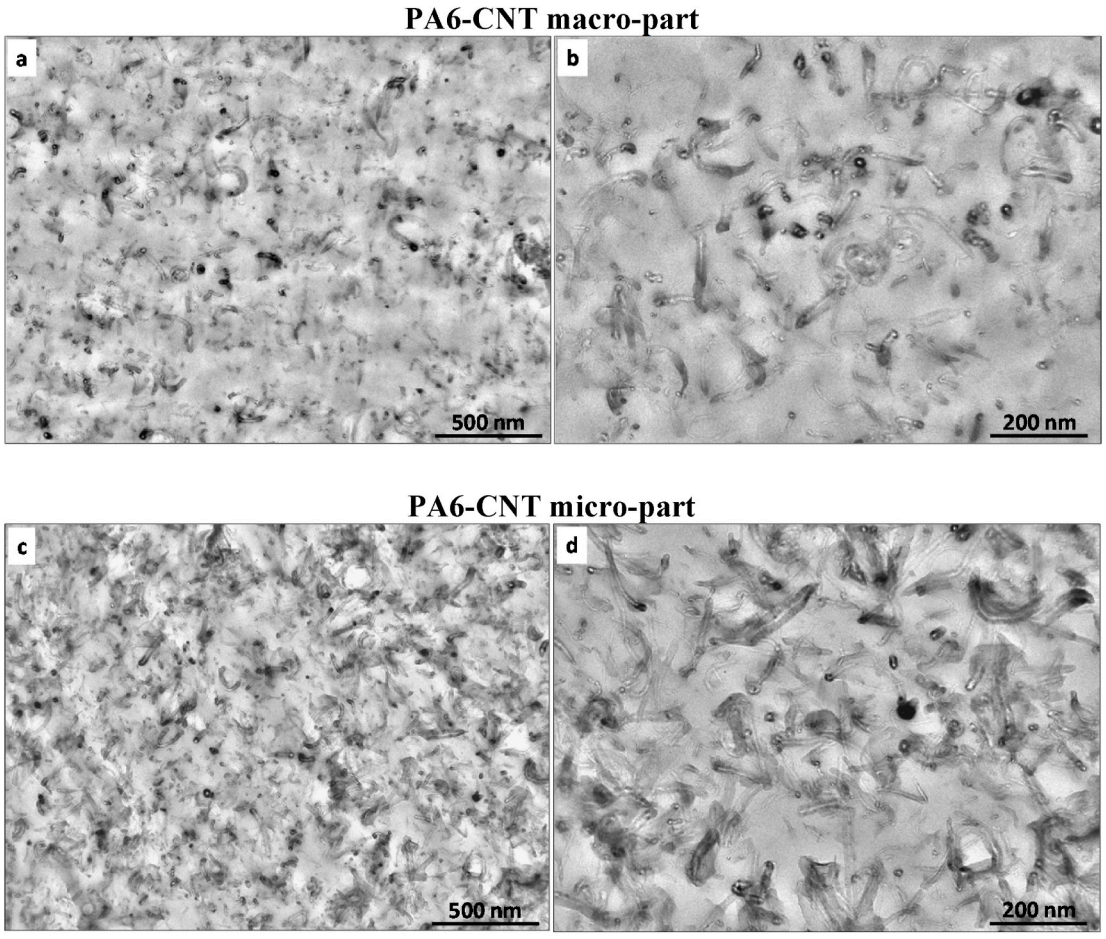

Fig. 5. TEM images of a macro- (**a** and **b**) and micro-part (**c** and **d**) made of PA6-CNT.

of isotropy. Particularly, the arc indicated by the arrow is attributed to the (001) diffraction plane of the γ crystalline phase. In summary, the 2D patterns of PA6 and PA6-MMT of micro-parts showed that crystals are oriented towards the flow direction. In addition, the scattering observed at low angle for the micro-part of PA6-MMT (marked by the dashed arrow), ascribed to the (001) diffraction plane of MMT, also indicates clearly that the clay platelets are oriented along the flow direction.

The micro-part of PA6-CNT does not show any sign of anisotropy.

Integrated intensity profiles have been computed from these patterns. A comparison of the diffractograms between macro- and micro-parts is reported in Fig. 8. The differences observed between macro- and micro-part appear quite similar for neat PA6 and PA6-MMT. More specifically, the micro-parts are predominantly under the γ form (characterized by the diffraction peak at $2\theta \approx 21.5^{\circ}$), while the macro-parts exhibit a mixture of both α and γ crystalline phases of PA6 (characteristic peaks of α form are located at $2\theta \approx 20^{\circ}$ and $2\theta \approx 24^{\circ}$). (Refer to Ref. [43] for the crystalline structure of PA6). The cooling rate of the melt is a well-known parameter that governs the crystalline phase of PA6. Particularly, a rapid cooling rate favors the formation of the γ phase while the α form is induced when the cooling rate decreases [44]. The results are, thus, in agreement with the literature and the predominance of the γ phase in the micro-parts of PA6 and PA6-MMT might be directly related to the faster cooling rate in the material in the micro-cavity, with respect to that in the macro-cavity. A different behavior is observed for PA6-CNT; only the α form is present in both macro- and micro-part. This is a clear indication that the fast cooling rate undergone by the material in the cavity is not a condition sufficient to promote the formation of the γ phase; we can reasonably assume that the differences in the processing conditions used in the micro-molding of the various materials play only a secondary role. The differences between the diffractograms of macro- and micro-part would be related to small differences in the interchain and intersheet distances characteristic of the crystals [45].

In order to highlight the possible effect of the nature of the filler (CNT and MMT) on the PA6 crystalline form in the nano-filled materials, WAXS analyses were performed on samples molten and then slowly cooled down to room temperature (see section 2.2.2). The results are reported in Fig. 9. After cooling from the melt at the same low cooling rate, PA6-MMT exhibits only the γ form, whereas PA6-CNT only the α form. This clearly evidences that MMT has a "γ nucleating effect" on PA6, in agreement with the literature [8,46]. Particularly, Miri et al. suggested that in such systems PA6 chains anchored to the platelets via their amide groups, and the H-bonded sheets of the γ-unit cell stand up onto the MMT platelets. Further, the "α nucleating effect" induced by CNT on PA6 presented in literature [47,48] is here confirmed.

The analysis of the low angle scattering region of MMT powder and of PA6-MMT micro- and macro-part ("face-on" direction) is depicted in Fig. 10. For MMT raw powder, a diffraction peak at $2\theta \approx 3.5^{\circ}$, characteristic of the basal plane (i.e. d_{001} plane), is observed, indicating that the inter-layer distance (d_{001} distance) is equal to ≈ 2.5 nm. For the macro-part, a shift of this peak to lower angles is noticed, indicating an intercalation of the macromolecules between the clay platelets; the d_{001} distance increases up to ≈3.2 nm. Finally, this distance is larger in the case of the micro-part, ≈ 3.7 nm. This result is in agreement with the distance, ≈ 4 nm, shown in the high magnification TEM pictures of the micro-part (Fig. 6f).

SAXS analyses have been performed in order to get an overview of the structure at the nanometer scale. The collected 2D-SAXS patterns

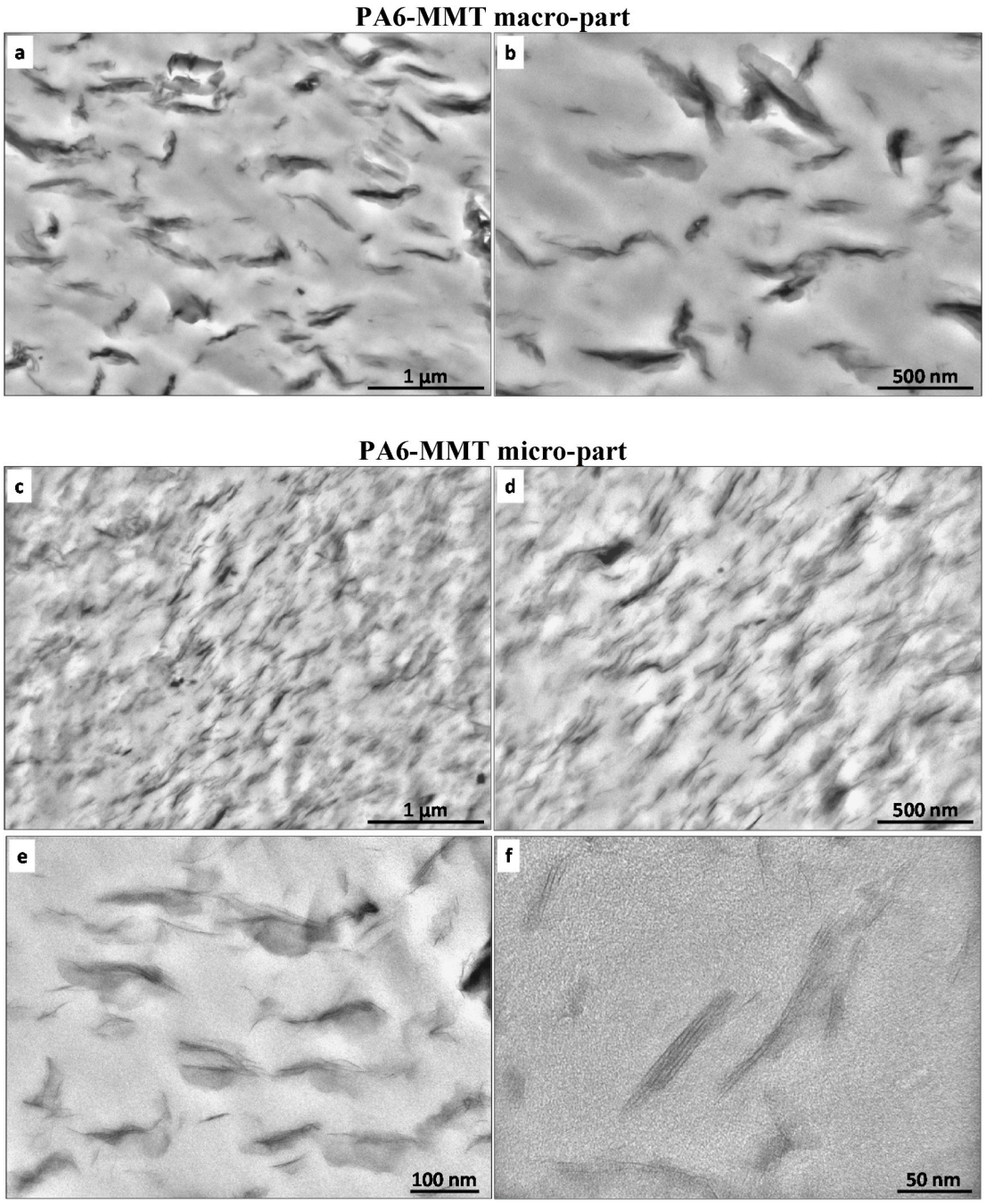

Fig. 6. TEM images obtained from macro- (**a** and **b**) and micro-part (**c**–**f**) made of PA6-MMT.

"face-on" are reported in Fig. 11. For the macro-part of neat PA6, a broad diffuse and isotropic scattering, characteristic of the long period (i.e. a regular stacking of the crystalline lamellae) is observed. By contrast, for the micro-part of PA6 this diffuse scattering rather turns toward spots indicating a preferred orientation of the crystalline structure along the flow direction. The long period values, calculated as $L_p = 2\pi/q_{max}$, with q_{max} the value of the maximum of the intensity in the $Iq^2 = f(q)$ plot, indicates a decrease from 8.8 nm for the macro-part to 7.2 nm for the micro-part. In addition, an intense horizontal central scattering is observed for the micro-part only. This scattering is characteristic of a fibrillary structure.

A similar response is observed for PA6-MMT. In addition, the central scattering, related to the scattering from the organo-clay, is isotropic for the macro-part, while it becomes anisotropic for the micro-part, indicating a preferred orientation of the clay platelets along the injection direction. As for neat PA6, a decrease in the L_p value from 8.1 nm to 6.3 nm is observed between the macro- and micro-part respectively.

Finally, regarding PA6-CNT, no appreciable difference is observed between macro- and micro-part and the majority of the intensity arises from the scattering from CNT. However, a detailed analysis of the patterns indicates a comparable long period for both macro- and micro-part (i.e. 7.6 nm vs 7.2 nm, respectively).

3.2.2. *Calorimetric response*

Fig. 12 shows the DSC melting endotherms of samples taken from micro- and macro-parts of neat PA6, PA6-MMT and PA6-CNT (one representative thermogram is reported for each part type and material); Table 3 summarizes the data from the scans.

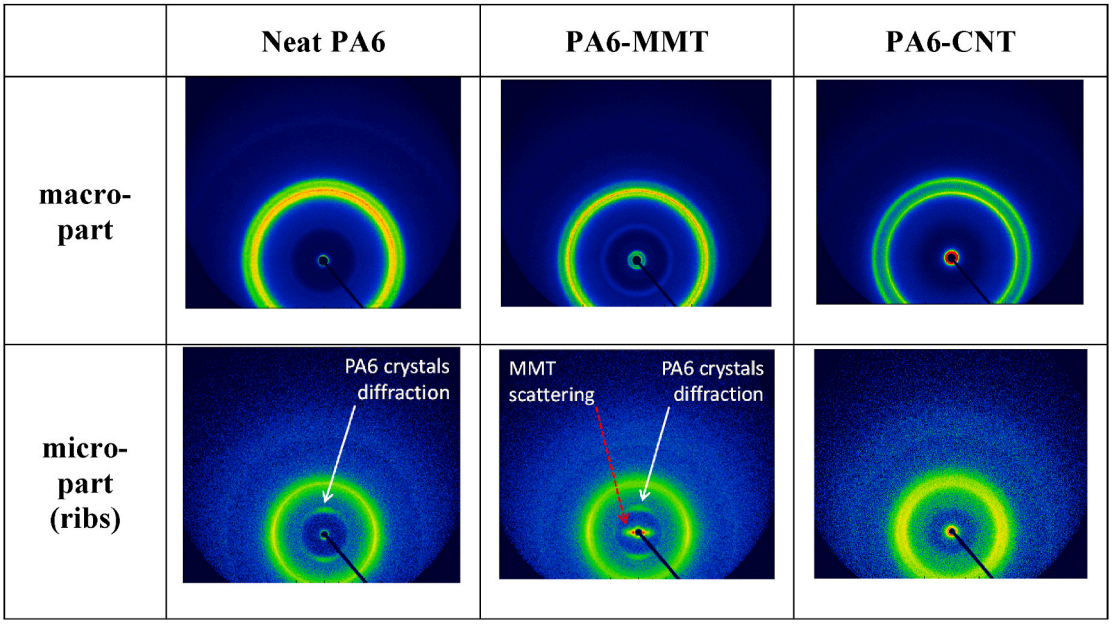

Figs. 7. 2D WAXS patterns of the macro- and micro-parts of neat and nano-filled PA6 (the "face-on" pattern is presented for the macro-parts).

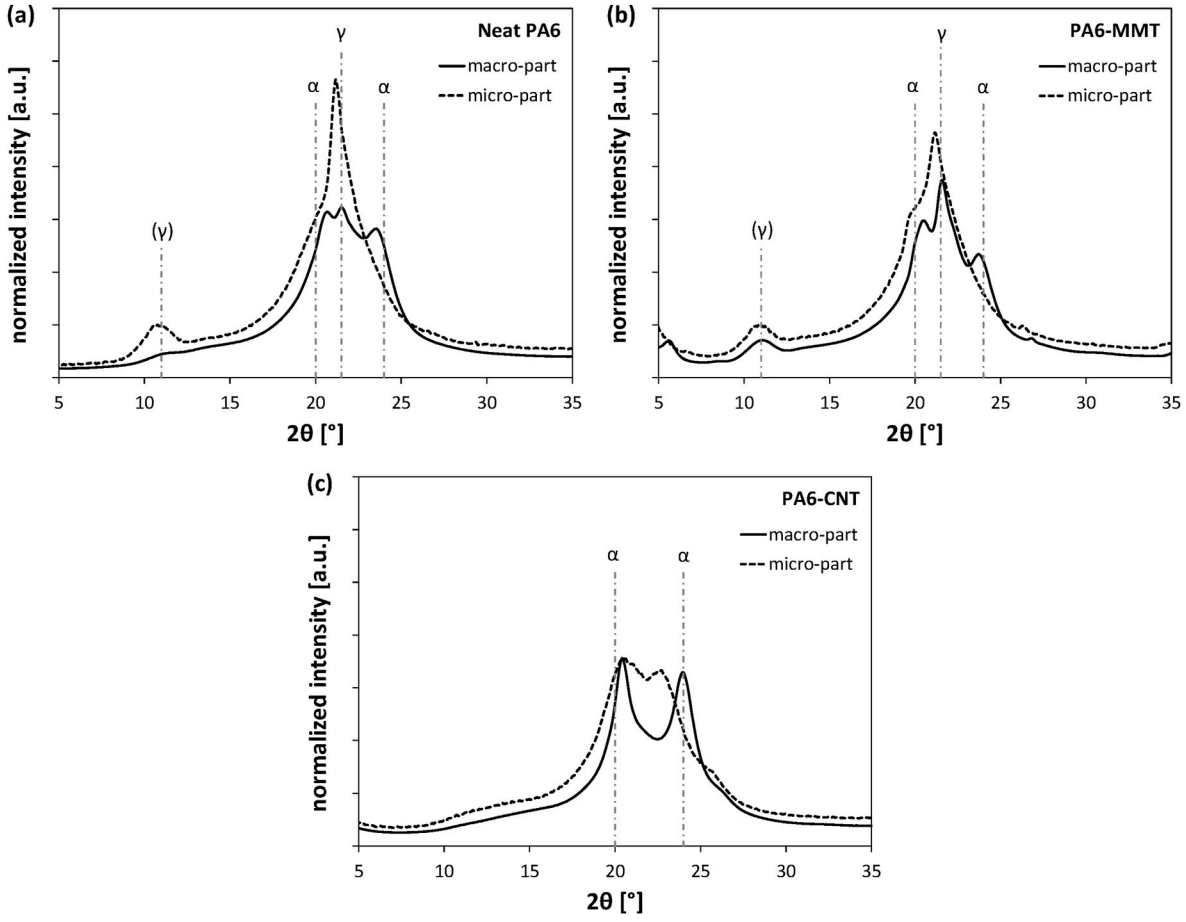

Fig. 8. WAXS diffractograms of the macro- and micro-parts of (**a**) neat PA6, (**b**) PA6-MMT and (**c**) PA6-CNT. Vertical dash-dot lines indicate the reference values of 2θ of α and γ crystalline phases of PA6 from literature [43].

The endothermic peak close to 220 °C, clearly visible in each scan, is associated to the fusion of α and γ crystalline phases of PA6 [8]. No appreciable difference is observed for the peak temperature (T_f in Table 3) among the various materials and parts examined. For PA6-MMT, a shoulder prior to the endothermic peak is clearly observed. This is generally associated with the γ crystalline form or with changes

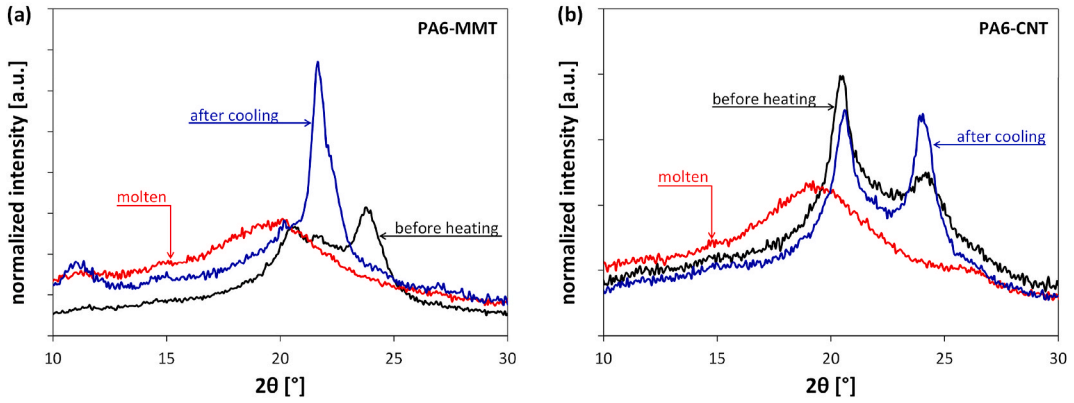

Fig. 9. WAXS diffractograms obtained from the heating/cooling experiments (see text) on (**a**) PA6-MMT and (**b**) PA6-CNT.

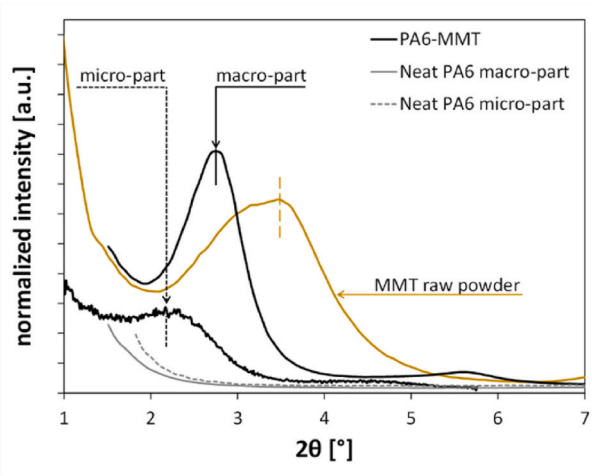

Fig. 10. Low angle WAXS diffractograms of the MMT powder and macro- and micro-parts made of PA6-MMT; the diffractograms of the neat PA6 macro- and micro-parts are also reported.

in crystallite thickness and distribution of the α form [8]. Considering that this shoulder is completely absent in the scans of PA6 and that WAXS analyses revealed the presence of the γ form in both PA6-MMT and PA6 parts, the shoulder observed in the PA6-MMT scans is more likely associated with the presence of imperfect α crystals, rather than the presence of the γ form. Crystals of this latter form do not produce any clearly detectable effect in the shape of the endothermic peaks here observed. However, it is worthy to notice that WAXS results can only guide the interpretation of DSC results, but, since they refer to samples in a different state, other effects might be relevant. Stress relaxation, moisture related effects and especially changes in crystalline structure can occur upon heating during the DSC experiment, which affect the results [50].

The broad exothermic peak that precedes the endothermic peak, ascribed to the fusion of PA6 α and γ crystalline phases, visible in all the thermograms of Fig. 12 except for the macro-part of PA6-CNT, is generally attributed to the cold crystallization of PA6 taking place during heating in the DSC experiment [50,51]. This exothermic peak indicates the presence, in the part, of regions where PA6 macromolecules rearranged in such a way to initiate crystal formation, but could not give rise to fully developed crystals since frozen by the rapid cooling in the mold. From Fig. 12 and Table 3, it emerges that cold crystallization occurs at a lower temperature (T_{cc} in Table 3) for the micro-part than for the macro-part, irrespective of the material examined (for

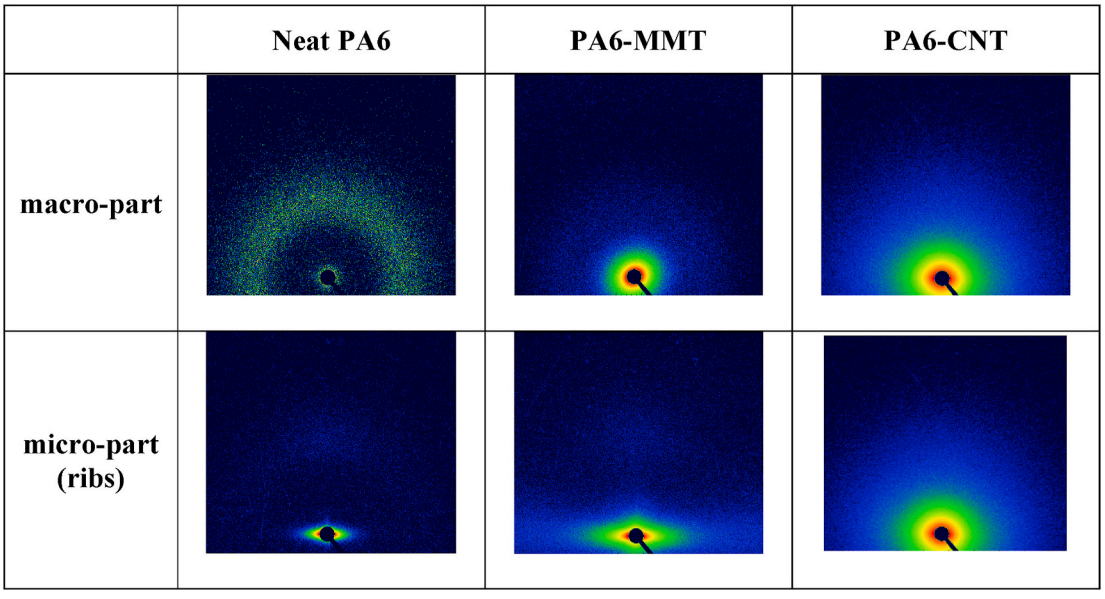

Fig. 11. 2D-SAXS patterns of the macro- and micro-parts of neat and nano-filled PA6 (the "face-on" pattern is presented for the macro-parts).

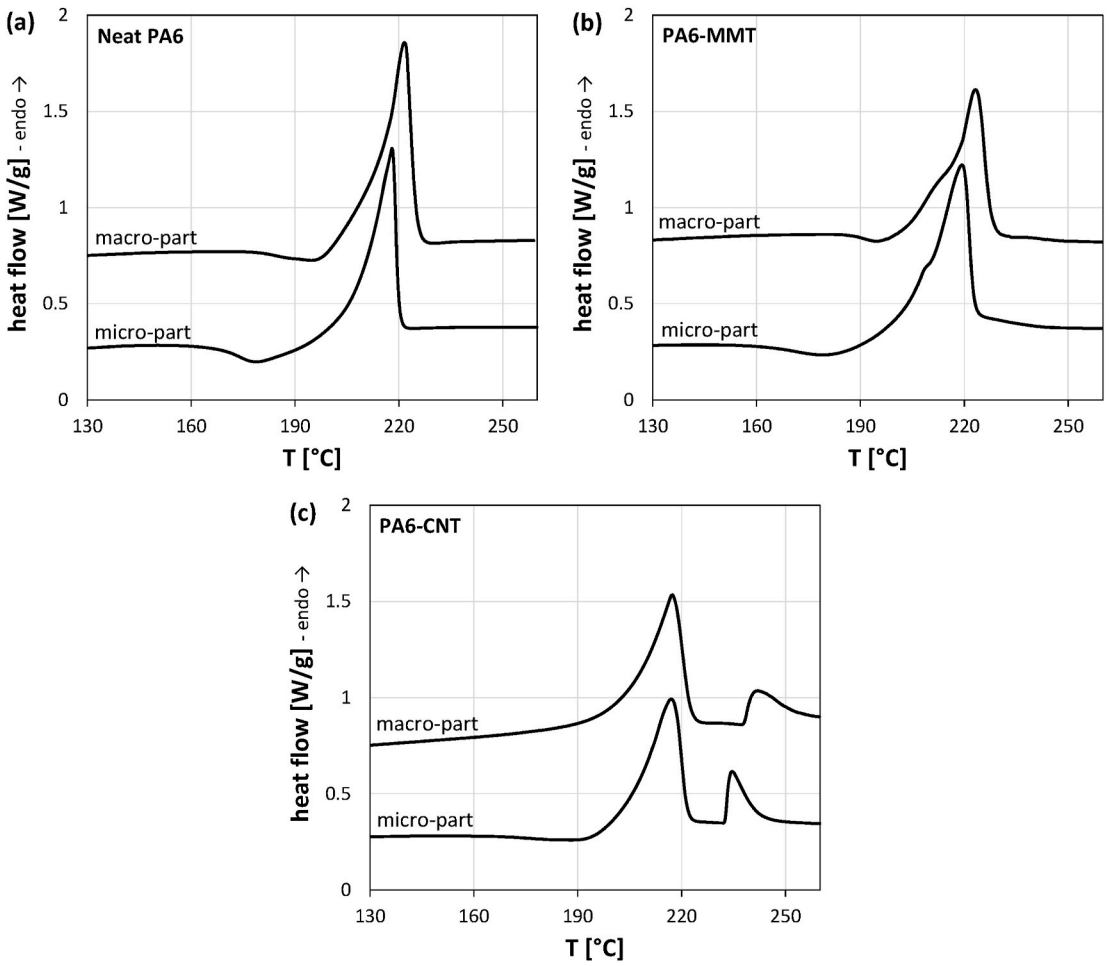

Fig. 12. DSC traces of the macro- and micro-parts of (**a**) neat PA6, (**b**) PA6-MMT and (**c**) PA6-CNT (one representative trace reported for each material/part combination). In each graph, the trace of the macro-part is shifted vertically for clarity.

Table 3
DSC data of the various materials/parts examined.

Material	samples from	# samples	T_{cc}[a] [°C]	ΔH_{cc}[a] [J/g]	T_f[b] [°C]	X_c[c] [%]	# T_{fh} samples	T_{fh}[d] [°C]
Neat PA6	micro-part (ribs)	3	179 ± 1	17 ± 2	218.1 ± 0.4	14.7 ± 0.5	0	–
	macro-part	3	191 ± 4	6 ± 1	220.9 ± 0.8	23.2 ± 0.4	0	–
PA6-MMT	micro-part (ribs)	3	182 ± 6	11.4 ± 0.2	220 ± 3	22 ± 3	1	228
	macro-part	5	193 ± 3	3 ± 2	221 ± 2	21 ± 2	0	–
PA6-CNT	micro-part (ribs)	3	186 ± 6	7 ± 1	217.2 ± 0.5	24 ± 3	2	240
	macro-part	3	-[e]	-[e]	219 ± 2	27 ± 1	3	245 ± 5

[a] Referred to the exothermic peak ascribed to PA6 cold crystallization taking place during heating in the DSC experiment; T_{cc} is the peak temperature; ΔH_{cc} is the specific enthalpy of crystallization of the polymer, determined as: $\Delta H_{cc} = \frac{\Delta H_{cc,s}}{1-f}$ where $\Delta H_{cc,s}$ is the specific enthalpy of the sample and f is the weight fraction of particles in the compound (f = 0 for the neat PA6).

[b] Referred to the endothermic peak close to 220 °C, directly related to the fusion of α and γ crystalline phases of PA6; T_f is the peak temperature.

[c] X_c is the overall crystallinity degree of the polymer, determined as: $X_c = \frac{\Delta H_{f,s} + \Delta H_{fh,s} - \Delta H_{cc,s}}{(1-f)\cdot \Delta H_f^0}$ where $\Delta H_{f,s}$ and $\Delta H_{fh,s}$ are the specific enthalpies of the sample related to the fusion of α and γ crystalline phases of PA6 (endothermic peak close to 220 °C) and to the high-temperature endothermic peak (see note d), respectively. ΔH_f^0 is the heat of fusion of the purely crystalline forms of PA6, assumed equal to 240 J/g [49].

[d] Referred to the high-temperature endothermic peak; T_{fh} is the peak temperature.

[e] Cold crystallization during heating in the DSC experiment not observed.

PA6-CNT, cold crystallization is observed only for the micro-part). In addition, the specific enthalpy associated to cold crystallization (ΔH_{cc} in Table 3) is higher for the former than for the latter. It is reasonable to relate the grater propensity at exhibiting cold crystallization of the micro-part to the faster cooling rate undergone by the material in the micro-cavity. The results indicate that the presence of CNT in the PA6 melt makes the material slightly prone to cold crystallization. For this system, in the macro-part, cold crystallization is not observed; in the micro-part it is detected at a higher temperature with respect to PA6 and PA6-MMT, and it exhibits a smaller enthalpy.

Interestingly, in some thermograms an endothermic peak can be noticed at a temperature higher than that of the peak ascribed to the

fusion of PA6 α and γ crystalline phases. This high-temperature endothermic peak has been detected for almost all samples of PA6-CNT examined, and one sample of PA6-MMT micro-part. For PA6-CNT samples (Fig. 12c), this peak is quite steep at its beginning and clearly distinguished from the endothermic peak around 220 °C and it was confirmed also by DSC analyses carried out with a different calorimeter, a DSC Q100 by TA Instruments (results not shown). Further analyses in which the sample was heated up to 260 °C, cooled down at 40 °C and then heated again up to 260 °C, revealed that this high-temperature peak can be observed only in the first heating scan. This indicates that it is due to a non-reversible process, directly related to the thermal history experienced by the material during the injection molding processes for the obtainment of the parts. The literature works report the formation of similar high-temperature endothermic peaks in PA6 thermograms only in presence of silicate layers [51,52] and relate it to the melting of very fine lamellae of PA6 formed in the confined environment on the surface of the silicates. A similar confining action might be promoted by CNT which are well dispersed within PA6, as indicated by TEM and WAXS analyses generating the high-temperature peak observed for examined the PA6-CNT samples. However, a comprehensive study of the process at the basis of this high-temperature peak would require additional specific analyses, which could be a matter of further studies.

The overall degree of crystallinity of the polymer (X_c) is also reported in Table 3. For PA6-CNT samples, the specific enthalpy associated to the high temperature endothermic peak was added to that ascribed to the fusion of the α and γ crystalline phases, while to obtain data more closely related to the material in the part, the specific enthalpy associated to cold crystallization was subtracted. The results show that, taking into account the standard deviations, an appreciable difference between micro-parts and macro-parts is noticed only for neat PA6, i.e. in absence of any secondary phase. More specifically, for the neat polymer, the thermal history experienced during the micro-molding leads to an overall degree of crystallinity that is remarkably lower than that obtained during macro-molding (the former is ≈ 60 % of the latter). For the nanocomposites, either in the form of micro- or macro-parts, similar values of X_c have been obtained.

4. Conclusions

In this work, the moldability via μIM of two nano-filled PA6 based systems, with the same nominal filler weight-content but different nature and geometry (carbon nanotubes, CNT, and silicate layers from organo-modified montmorillonite, MMT, respectively), was investigated and compared with traditional IM. A micro-rib with cross-section of 0.03 mm^2 and a standard dumbbell specimen for tensile tests were used as reference micro- and macro-injected part; the cross-section of the macro-part was ≈1300 times that of the micro-part. The microstructural characteristics of the materials in the two different parts were then analyzed and compared.

To obtain regular quality micro-parts, the μIM process parameters had to be selected according to the material examined; whereas regular quality macro-parts could be obtained for the various materials using the same IM process conditions. This was directly related to the fact that the thermomechanical histories experienced by the material in the two different IM processes were largely different. Once optimized the process conditions, the presence of nano-fillers did not impair the mold replication capability of PA6 nanocomposites in the μIM process.

The different thermomechanical histories during μIM and IM brought to different microstructural characteristics depending also largely on the material.

Micro- and macro-parts show a homogenous and comparable CNT dispersion without any preferential orientation. By contrast, PA6-MMT shows a big difference between micro- and macro-part. In the former MMT particles appeared much smaller in size and characterized by a higher degree of intercalation of PA6 macromolecules and the presence of individual silicate layers coming from exfoliation processes was clearly detected. Further, a preferential orientation of the MMT particles along the flow direction in the cavity was observed in the micro-part.

With regard to the PA6 crystallinity, minor differences between micro- and macro-parts were noticed for PA6-CNT. For this system, no preferential orientation was observed for the PA6 crystals, which appeared of the α form irrespective of the part type. On the contrary, for both neat PA6 and PA6-MMT, the structural characteristics of PA6 crystals appeared remarkably different in the two types of part: only in the micro-part a pronounced orientation was observed for the PA6 crystals (along the flow direction), together with a clear propensity to develop the γ crystalline phase of PA6 to the detriment of the α form. Interestingly, the presence of either CNT or MMT particles prevented the decrease of the overall degree of crystallinity of PA6 observed in micro-part made of neat PA6.

In conclusion, this paper clearly highlights that the two nanocomposites here examined can be successfully processed by μIM to fabricate high-value micro-components. Further, for the design of these micro-injected parts, referring to material properties measured on standard IM parts can be possible only for some composites. Indeed, CNT homogeneously dispersed in a low-viscosity PA6 matrix were able to overcome the effects induced by the thermomechanical history experienced by the material during the μIM process, showing the same material microstructure despite of the large difference in size of the examined part.

CRediT authorship contribution statement

Rossella Surace: Conceptualization, Methodology, Investigation, Writing, Supervision. **Claudia Pagano:** Conceptualization, Methodology, Investigation, Writing, Supervision. **Vincenzo Bellantone:** Conceptualization, Methodology, Investigation, Writing, Supervision. **Simone Gatti:** Resources, Investigation. **Leonardo Castellani:** Methodology, Investigation. **Massimo Vighi:** Methodology, Investigation. **Grégory Stoclet:** Methodology, Investigation, Writing. **Sara Sechi:** Methodology, Investigation. **Irene Fassi:** Funding acquisition. **Francesco Baldi:** Conceptualization, Methodology, Investigation, Writing, Supervision.

Declaration of competing interest

The authors declare that they have no known competing financial interests or personal relationships that could have appeared to influence the work reported in this paper.

Acknowledgments

The authors are grateful to Ms. Isabella Peroni and Ms. Gloria Spagnoli of Dipartimento di Ingegneria Meccanica e Industriale of Università degli Studi di Brescia (Italy) for the support in the execution of the thermal tests. The financial support from Région Nord Pas-de-Calais and European FEDER for SAXS laboratory equipment is also gratefully acknowledged.

APPENDIX. Mechanical properties of the materials from tests on the macro-parts

Uniaxial tensile tests were carried out on the macro-parts, which consisted in the dumbbell specimens for standard tensile tests (described in section 2.1.2), in order to get an overview of the stress-strain behavior of the materials examined.

The tests were performed using a Universal Testing System by Instron (model 3366), equipped with a 10 kN load cell, at room temperature. For the measurement of strength and ductility, the crosshead speed was set at 10 mm/min. From each test, the material nominal stress-strain curve was recorded, and the yield stress and the elongation at break were determined. For the measurement of the stiffness (Young's modulus), the experiments were carried out at 1 mm/min, with a strain-gauge extensometer (with a gauge length of 10 mm). Since the mechanical properties of PA6 are strongly influenced by the water content, the specimens were pre-dried before the test. They were kept in an oven at 80 °C, under vacuum, for 17 h. Once pre-dried, they were stored in a desiccator under vacuum at room temperature and tested on the same day. Three samples for each material were analyzed.

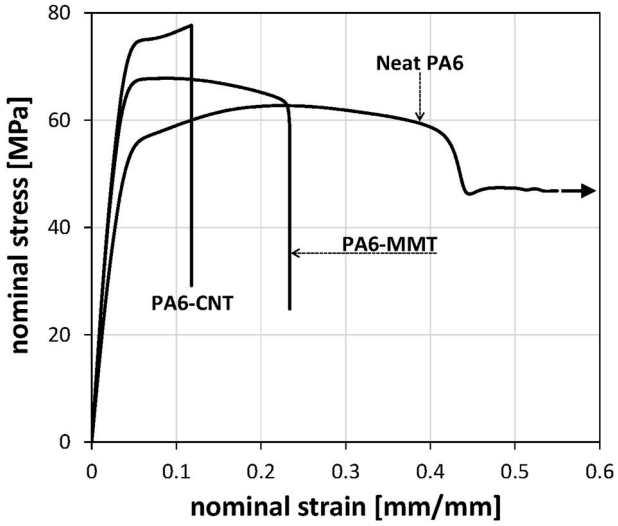

Fig. A1. Representative nominal stress-strain curves of the materials from tests on the macro-parts (pre-dried materials).

The stress-strain curves of neat PA6, PA6-MMT and PA6-are reported in Fig. A1 CNT (one representative curve for each material). Table A1 reports the tensile properties. It clearly emerges that the nano-fillers promote an increase in the Young's modulus and strength (yield stress) and a reduction in the ductility (elongation at break), with respect to the neat PA6. For PA6-CNT the effects are more marked. Interestingly, for both the nano-filled systems, the embrittlement induced by the nano-fillers is not so pronounced to completely suppress yielding under tensile loading. This finding is in contrast with what is typically observed for nanocomposites with similar filler content (7%wt.), at least those containing organo-clay particles (see, for example [53]). Overall, the nanocomposites here examined show a good mechanical response that would make them suitable for the production of high value mechanical engineering parts. To conclude, it should be pointed out that for neat PA6 and PA6-MMT, in consideration of the differences in the microstructure between micro- and macro-parts, it is not expected that material stiffness and strength in the micro-part comply with those here presented. By contrast, for PA6-CNT, for which only minor differences have been noticed between micro- and macro-parts, the levels of stiffness and strength measured on the macro-part might be considered valid also for the material in the micro-part.

Table A1
Tensile properties of the various materials from tests on the macro-parts (pre-dried materials). For each property, the mean value ± standard deviation evaluated from test repetitions (three samples) is reported.

Material	Young's modulus[a] [GPa]	Yield stress [MPa]	elongation at break [%]
Neat PA6	2.8 ± 0.3	53 ± 2	>100[b]
PA6-MMT	3.9 ± 0.5	65 ± 3	23.5 ± 0.4
PA6-CNT	4.7 ± 0.2	72 ± 3	10 ± 3

[a] tests carried out with the extensometer.
[b] higher than 100 %.

References

[1] Z. Tadmor, C.G. Gogos, Principles of Polymer Processing, second ed., John Wiley & Sons, Hoboken, 2006.
[2] S. Hashemi, J. Mugan, Fracture mechanics of short glass fibre-reinforced nylon composites, J. Mater. Sci. 28 (1993) 3983–3990.
[3] D.M. Laura, H. Keskkula, J.W. Barlow, D.R. Paul, "Effect of glass fiber and maleated ethylene–propylene rubber content on tensile and impact properties of Nylon 6", Polymer 41 (2000) 7165–7174.
[4] S. Fara, A. Pavan, Fibre orientation effects on the fracture of short fibre polymer composites: on the existence of a critical fibre orientation on varying internal material variables, J. Mater. Sci. 39 (2004) 3619–3628.
[5] J. Tiusanen, D. Vlasveld, J. Vuorinen, Review on the effects of injection moulding parameters on the electrical resistivity of carbon nanotube filled polymer parts, Compos. Sci. Technol. 72 (2012) 1741–1752.
[6] L. Peponi, D. Puglia, L. Torre, L. Valentini, J.M. Kenny, "Processing of nanostructured polymers and advanced polymeric based nanocomposites" Materials, Science and Engineering R 85 (2014) 1–46.
[7] G. Mittal, V. Dhand, K.Y. Rhee, S.-J. Park, W.R. Lee, A review on carbon nanotubes and graphene as fillers in reinforced polymer nanocomposites", J. Ind. Eng. Chem. 21 (2015) 11–25.
[8] T.D. Fornes, D.R. Paul, Crystallization behavior of nylon 6 nanocomposites, Polymer 44 (2003) 3945–3961.
[9] S. Zhou, A.N. Hrymak, M.R. Kamal, "Electrical, morphological and thermal properties of microinjection molded polyamide 6/multi-walled carbon nanotubes nanocomposite" Composites Part A, Applied Science and Manufacturing 103 (2017) 84–95.
[10] N. Bumbudsanpharoke, W. Lee, J.C. Choi, S.-J. Park, M. Kim, S. Ko, Influence of Montmorillonite nanoclay content on the optical, thermal, mechanical and barrier properties of low-density polyethylene, Clays and clay Mineral 65 (2017) 387–397.
[11] J. Szakacs, R. Petreny, L. Meszaros, Crystalline properties of melt-processed polyamide 6 matrix multiscale hybrid composites, J. Therm. Anal. Calorim. 137 (2019) 43–53.
[12] T.D. Fornes, P.J. Yoon, H. Keskkula, D.R. Paul, Nylon 6 nanocomposites: the effect of matrix molecular weight", Polymer 42 (2001) 9929–9940.
[13] F. Baldi, A. Franceschini, F. Bignotti, G. Tieghi, T. Ricco, Rheological behaviour of nano-composites based on polyamide 6 under shear and elongational flow at high strain rates, Rheol. Acta 48 (2009) 73–88.

[14] M.D. Via, F.A. Morrison, J.A. King, J.A. Caspary, O.P. Mills, G.R. Bogucki, Comparison of rheological properties of carbon nanotube/polycarbonate and carbon black/polycarbonate composites, J. Appl. Polym. Sci. 121 (2011) 1040–1051.

[15] I. Fassi, D. Shipley (Eds.), Micro-manufacturing Technologies and Their Applications: a Theoretical and Practical Guide, Springer, 2018.

[16] G. Trotta, A. Volpe, A. Ancona, I. Fassi, Flexible micro manufacturing platform for the fabrication of PMMA microfluidic devices, J. Manuf. Process. 35 (2018) 107–117.

[17] D. Loaldi, D. Quagliotti, M. Calaon, P. Parenti, M. Annoni, G. Tosello, Manufacturing signatures of injection molding and injection compression molding for micro-structured polymer fresnel lens production, Micromachines 9 (2018) 653.

[18] N. Milan, M. Sorgato, P. Parenti, M. Annoni, G. Lucchetta, Effects of micromilled NiP mold surface topography on the optical characteristic of injection molded prismatic retroreflectors, Precis. Eng. 61 (2020) 126–135.

[19] M. Zhou, X. Xiong, B. Jiang, C. Weng, Fabrication of high aspect ratio nanopillars and micro/nano combined structures with hydrophobic surface characteristics by injection molding, Appl. Surf. Sci. 427 (2018) 854–860.

[20] W. Yu, S. Ruan, Z. Li, J. Gu, X. Wang, C. Shen, B. Chen, Effect of injection velocity on the filling behaviors of microinjection-molded polylactic acid micropillar array product, Int. J. Adv. Manuf. Technol. 103 (2019) 2929–2940.

[21] W.-B. Kim, S.-Y. Han, Microinjection molding of out-of-plane bistable mechanisms, Micromachines 11 (2020) 155.

[22] J. Giboz, T. Copponnex, P. Mélé, Microinjection molding of thermoplastic polymers: a review, J. Micromech. Microeng. 17 (2007) R96.

[23] Z. Lu, K.F. Zhang, Morphology and mechanical properties of polypropylene micro-arrays by micro-injection molding, Int. J. Adv. Manuf. Technol. 40 (2009) 490, https://doi.org/10.1007/s00170-007-1364-6.

[24] J. Giboz, A.B. Spoelstra, G. Portale, T. Copponnex, H.E.H. Meijer, G.W.M. Peters, P. Mélé, "On the origin of the "Core-Free'' morphology in microinjection-molded HDPE", J. Polym. Sci. B Polym. Phys. 49 (2011) 1470–1478.

[25] C. Guo, F.H. Liu, X. Wu, H. Liu, J. Zhang, Morphological evolution of HDPE parts in the microinjection molding: comparison with conventional injection molding, J. Appl. Polym. Sci. 126 (2012) 452–462.

[26] F. Baldi, A. Bongiorno, I. Fassi, A. Franceschini, C. Pagano, T. Ricco, R. Surace, F. Tescione, Process–property–structure relationship in miniaturized injection moulded polyoxymethylene samples", Polym. Eng. Sci. 54 (2014) 512–521.

[27] D. Annicchiarico, J.R. Alcock, Review of factors that affect shrinkage of molded part in injection molding, Mater. Manuf. Process. 29 (6) (2014) 662–682, https://doi.org/10.1080/10426914.2014.880467.

[28] J. Jiang, S. Wang, B. Sun, S. Ma, J. Zhang, Q. Lia, G.-H. Hu, Effect of mold temperature on the structures and mechanical properties of micro-injection molded polypropylene, Mater. Des. 88 (2015) 245–251.

[29] D. Mi, R. La, W. Chen, J. Zhang, "Different kinds of transcrystallinity developed from glass fiber/isotactic polypropylene/β-nucleation agents composite by microinjection molding", Polym. Adv. Technol. 27 (9) (2016) 1220–1227.

[30] S. Shi, L. Wang, Y. Pan, C. Liu, X. Liu, Y. Li, J. Zhang, G. Zheng, Z. Guo, Remarkably Strengthened microinjection molded linear low-density polyethylene (LLDPE) via multi-walled carbon nanotubes derived nanohybrid shish-kebab structure, Compos. B Eng. 167 (2019) 362–369.

[31] A. Bongiorno, C. Pagano, F. Baldi, V. Bellantone, R. Surace, I. Fassi, "Micro-injection molding of CNT nanocomposites obtained via compounding process", Polym. Compos. 38 (2) (2017) 349–362.

[32] ISO 527-1:2019 Plastics - Determination of Tensile Properties - Part 1: General Principles.

[33] Sumitomo (SHI) Demag Plastics Machinery GmbH, Technical description, available at: www.sumitomo-shi-demag.eu.

[34] G. Tosello, H.N. Hansen, B. Dormann, C. Decker, P. Guerrier, "Process control and product evaluation in micro molding using a screwless/two-plunger injection unit", Proceedings of ANTEC 2010; Orlando, Florida USA; 2161-2166.

[35] R. Surace, V. Bellantone, G. Trotta, I. Fassi, Replicating capability investigation of micro features in injection moulding process, J. Manuf. Process. 28 (2017) 351–361.

[36] ISO 294-4:2018 Plastics - Injection Moulding of Test Specimens of Thermoplastic Materials - Part 4: Determination of Moulding Shrinkage.

[37] M.S. Huang, J.C. Li, Y.M. Huan, L.C. Hsieh, Robust parameter design of micro-injection molded gears using a LIGA-like fabricated mold insert, J. Mater. Process. Technol. 20 (2009), 5690-570.

[38] U.M. Attia, J. Alcock, Optimising process conditions for multiple quality criteria in micro-injection moulding, Int. J. Adv. Manuf. Technol. 50 (2010) 533–542.

[39] V. Bellantone, R. Surace, G. Trotta, I. Fassi, Replication capability of micro injection moulding process for polymeric parts manufacturing, Int. J. Adv. Manuf. Technol. 6 (2013) 1407–1421.

[40] M.R. Mani, R. Surace, P. Ferreira, J. Segal, I. Fassi, S. Ratchev, Process parameters effect on dimensional accuracy of micro-injection moulded part, J Micro-Nano Mfg 1 (3) (2013), 031003-1-8.

[41] F.P. La Mantia, R. Marino, N.T. Dintcheva, Morphology modification of polyethylene/clay nanocomposite samples under convergent flow, Macromol. Mater. Eng. 294 (2009) 575–581.

[42] E. Mitsoulis, M. Battisti, A. Neunhäuserer, L. Perko, W. Friesenbichler, Flow behavior of PP-polymer nanocomposites in injection molding hyperbolical dies, Adv. Polym. Technol. 37 (2018) 3045–3055.

[43] J.P. Parker, P.H. Lindenmeyer, On the crystal structure of nylon 6, J. Appl. Polym. Sci. 21 (3) (1977) 821–837, https://doi.org/10.1002/app.1977.070210322.

[44] V. Brucato, G. Crippa, S. Piccarolo, G. Titomanlio, Crystallization of polymer melts under fast cooling. I: nucleated polyamide 6, Polym. Eng. Sci. 31 (1991) 1411–1416.

[45] Y. Zhang, Yi Zhang, S. Liu, A. Huang, Z. Chi, J. Xu, J. Economy, Phase stability and melting behavior of the α and γ phases of Nylon 6, J. Appl. Polym. Sci. 120 (2011) 1885–1891.

[46] V. Miri, S. Elkoun, F. Peurton, C. Vanmansart, J.-M. Lefebvre, P. Krawczak, R. Seguela, Crystallization kinetics and crystal structure of nylon6-clay nanocomposites: combined effects of thermomechanical history, clay content, and cooling conditions, Macromolecules 41 (2008) 9234–9244.

[47] E. Logakis, C. Pandis, V. Peoglos, P. Pissis, C. Stergiou, J. Pionteck, P. Potschke, M. Micusik, M. Omastova, "Structure–Property relationships in polyamide 6/multi-walled carbon nanotubes nanocomposites", J. Polym. Sci. B Polym. Phys. 47 (2009) 764–774.

[48] J. Szakacs, R. Petreny, L. Meszaros, Crystalline properties of melt-processed polyamide 6 matrix multiscale hybrid composites, J. Therm. Anal. Calorim. 137 (2019) 43–53.

[49] K.H. Illers, Polymorphism, crystallinity, and melting enthalpy of poly(epsilon-caprolactam) .2. Calorimetric investigations, Makromol. Chem. 179 (2) (1978) 497–507.

[50] Y.P. Khanna, W.P. Kuhn, Measurement of crystalline index in nylons by DSC: complexities and recommendations, J. Polym. Sci., Part B: Polym. Phys. 35 (14) (1997) 2219–2231.

[51] A. Yebra-Rodriguez, P. Alvarez-Lloret, C. Cardell, A.B. Rodriguez-Navarro, Crystalline properties of injection molded polyamide-6 and polyamide-6/montmorillonite nanocomposites, Appl. Clay Sci. 43 (2009) 91–97.

[52] Xiao Hu, Xiongyan Zhao, Effects of annealing (solid and melt) on the time evolution of polymorphic structure of PA6/silicate nanocomposites, Polymer 45 (11) (2004) 3819–3825.

[53] F. Baldi, F. Bignotti, G. Tieghi, T. Ricco, Rubber toughening of polyamide 6/organoclay nanocomposites obtained by melt blending, J. Appl. Polym. Sci. 99 (2006) 3406–3416.